



# Self-constructed carbon nanoparticles-coated porous biocarbon from plant moss as advanced oxygen reduction catalysts



Lihua Zhou<sup>a</sup>, Peng Fu<sup>a,b</sup>, Dehuang Wen<sup>a</sup>, Yong Yuan<sup>b,\*</sup>, Shungui Zhou<sup>c</sup>

<sup>a</sup> School of Chemical Engineering and Light Industry, Guangdong University of Technology, Guangzhou 510006, China

<sup>b</sup> Guangdong Key Laboratory of Agricultural Environment Pollution Integrated Control, Guangdong Institute of Eco-Environmental and Soil Sciences, Guangzhou 510650, China

<sup>c</sup> College of Resources and Environment, Fujian Agriculture and Forestry University, Fuzhou 350002, China

## ARTICLE INFO

### Article history:

Received 14 April 2015

Received in revised form 3 July 2015

Accepted 17 August 2015

Available online 21 August 2015

### Keywords:

Carbon nanoparticles

Porous biocarbon

Moss

Electrocatalyst

Oxygen reduction reaction

## ABSTRACT

The development of inexpensive metal-free catalysts with high activity and stability as substitutes for carbon-supported platinum catalysts (Pt/C) in the oxygen reduction reaction (ORR) remains a great challenge. In this paper, we report a novel type of self-constructed, carbon nanoparticle (CNP)-coated porous biocarbon prepared from a natural, readily available, and renewable plant moss (*Weisiopsis anomala*) with single precursor using template-free heat treatment. The CNPs were self-sponsored from the moss, which were simultaneously self-packed on the moss-derived carbon matrix via strong interactions between the hydroxyl and carbonyl functional groups of the CNPs and the moss-derived carbon matrix during the hydrothermal treatment. After being further carbonized at 900 °C, the moss-derived, CNP-coated biocarbon material had a larger surface area than that of the CNP-free, moss-derived biocarbon material. Electrochemical characterization showed that the CNP-coated biocarbon had a high activity in the ORR with an onset potential of 0.935 V vs. the reversible hydrogen electrode (RHE); this value is close to that of a commercial Pt/C catalyst (0.962 V vs. RHE) and is more positive than that of a CNP-free biocarbon material. The CNP-coated biocarbons also displayed a high limited current density, excellent long-term stability and resistance to methanol crossover, offering performance characteristics superior to those of Pt/C. Moreover, a microbial fuel cell (MFC) equipped with a CNP-coated biocarbon cathode outperformed an MFC with a Pt/C cathode in terms of energy output. This study presents a new approach for the production of inexpensive nanostructured carbon materials that exhibit high performance in the ORR from a natural resource.

© 2015 Elsevier B.V. All rights reserved.

## 1. Introduction

The oxygen reduction reaction (ORR), one of the key reactions occurring at the cathode in fuel cells, determines the performance of an energy-conversion device [1–3]. Because the reaction rate of the ORR is often sluggish, active catalysts are required to accelerate it. Platinum (Pt)-based materials are the most efficient ORR catalysts because of their high catalytic activities, but their scarcity, high cost, and low tolerance of Pt to poisoning have hindered their use in fuel cells [4,5]. Moreover, decreases in fuel cell performance have often been observed because of decreases in ORR activity due to the gradual loss of the electrochemical surface area of Pt-based materials [6,7]. Thus, alternatives to Pt-based electrocatalysts that have high performance and durability are highly desired.

Recently, nitrogen-doped carbonaceous materials have been extensively investigated as ideal candidates to replace Pt-based materials because of their excellent ORR electrocatalytic performance, low cost, high tolerance to fuel poisoning and long-term stability [8–11]. For N-doped carbon materials, their high activities in the ORR can be ascribed to the presence of graphitic, pyridinic and pyrrolic-like N species [12,13]. The N atoms in the carbon structures can attract electrons from the carbon atoms, creating a positive charge density on the adjacent C atoms and resulting in the highly favorable adsorption of O<sub>2</sub> [14]. Numerous studies have demonstrated that efficient N-doped, carbon-based catalysts can be prepared using carbon nanotubes and graphene as hosts and N-enriched chemicals (e.g., melamine, urea, and NH<sub>3</sub>) as nitrogen sources [15,16]. N-doped carbon catalysts can also be produced using soft- or hard-template carbonization methods with C- and N-enriched chemicals as precursors [17,18]. However, the sources of N/C are relatively expensive and harmful, and the synthetic procedures used to prepare these catalysts are tedious. Thus, the

\* Corresponding author.

E-mail address: [yuanyong@soil.gd.cn](mailto:yuanyong@soil.gd.cn) (Y. Yuan).

large-scale production of such materials by these methods has been limited.

Recently, varieties of natural biomass derived from plants and animals have been transformed into N-doped carbon materials and utilized as efficient catalysts in the ORR. Biomass-derived, N-doped carbon catalysts can be produced in sufficient quantities at a relatively low cost, and they represent a promising potential alternative to conventional catalysts. Numerous N-doped carbon materials derived from biomass, such as seaweed, Amaranthus, microorganisms, *Typha orientalis*, bamboo fungus, bacterial cellulose and okara, have been produced, and they have shown significant potential as catalysts in the ORR [19–25]. It is desirable for catalysts to possess nanoscale porosity and a relatively high content of N groups; these properties lead to high mass transfer fluxes and the existence of a large number of active sites. Therefore, chemical activation or post-treatment in ammonia gas is frequently applied to introduce porous structures and N groups into biomass-derived carbon materials [22–25], but these methods also require massive use of expensive or harmful chemicals. Moreover, the as-prepared carbonaceous materials are not nanostructured, a property that is beneficial in catalytic reactions.

In this study, we demonstrate a facile, self-assembly-based approach that can be used to produce nanostructured, N-doped carbon materials from plant moss via a two-step heat treatment process. Moss, a phylum of small and soft plants, is one of the most abundant plant species, covering approximately 3% of the Earth's surface. Moss is well known for its water-holding ability because of the open macroscopic cellular structure of its leaves [26]. A survey of the existing literature reveals that only one group has thus far reported the use of moss-derived biocarbon materials in electrochemical applications. Ding et al. reported the conversion of peat moss into three-dimensional macroporous interconnected networks of carbon nanosheets and the use of this material as sodium ion battery anodes [27]. The group used a mild air activation step to increase the porosity of the moss-derived carbon to improve its performance in the battery. In contrast to the various woods that are cellulose-rich, moss contains high contents of hemicelluloses, lignins, carbohydrates, and amino acids that can lead to highly favorable carbon architectures during heat treatments [28]. Herein, we fully exploit the chemical composition of moss. By combining low-temperature hydrothermal carbonization with high-temperature pyrolysis, this virtually inexhaustible biomass was converted into a novel nanostructured, N-doped porous biocarbon material that displayed excellent activity in the ORR.

## 2. Experimental methods

### 2.1. Preparation of self-constructed, carbon nanoparticle (CNP)-coated, N-doped porous biocarbon materials

Moss (*Weisiopsis anomala*) was obtained from local concrete walls (Fig. S1), and it was washed with distilled water. In a typical synthesis in which CNP-coated, N-doped porous carbon was prepared from moss (Fig. 1a), 1.0 g of raw moss was transferred into a 25-mL Teflon-lined stainless steel vessel containing 20 mL of deionized water. This mixture was heated at 180 °C for 24 h, and then it was allowed to cool to ambient temperature. The resultant brownish solid product (named HMC180) was separated from the solution via centrifugation. The remaining solution was collected for further measurement, and it was shown to contain water-soluble carbon nanodots. The resultant HMC180 was then heated at high temperatures in an alumina crucible under a N<sub>2</sub> atmosphere for 2 h to generate the final carbon catalysts. The generated carbon materials were labeled TMC700, TMC800, TMC900, and TMC1000, respectively, representative of their annealing temperatures. For

comparison, moss was also annealed directly at 900 °C under a N<sub>2</sub> atmosphere for 2 h without hydrothermal pretreatment; this sample was termed AMC900. In addition, HMC180 was treated with ultrasound for 2 h to remove the attached CNPs and then annealed at 900 °C; the resulting sample was labeled U-TMC900 (Fig. 1a). Prior to electrochemical measurement, the black carbon materials collected from the furnace were treated with 1.0 M HCl and hot deionized water to remove the metal components and then dried at 60 °C overnight.

### 2.2. Structural characterization

The morphologies and structures of the as-prepared carbon materials were characterized using a field-emission scanning electron microscope (FE-SEM, model S-4800, Hitachi, Ltd., Tokyo, Japan) and a high-resolution analytical transmission electron microscope (HRTEM, model 2010, JEOL, Ltd., Tokyo, Japan). N<sub>2</sub> adsorption isotherms were measured at 77 K on a sorptometer (Model 1800, Carlo Erba Instruments, Italy). The specific surface areas were calculated using the Brunauer–Emmett–Teller (BET) method. X-ray photoelectron spectroscopy (XPS) measurements were performed using an X-ray photoelectron spectrometer (XPS, Kratos Model XSAM800) with a monochromatic Mg X-ray source. Fourier transform infrared (FTIR) spectra were recorded on a Hitachi EPI Infrared Spectrophotometer using the KBr disk method. Fluorescence spectra were obtained using a fluorescence spectrometer (PerkinElmer LS45).

### 2.3. Electrochemical measurements

The electrochemical characteristics of the carbon materials were determined using a conventional three-electrode cell system on an electrochemical workstation (CHI600D, Shanghai Chenhua Instruments Co., China). A glassy carbon (GC) disk with a diameter of 5.0 mm (after electrocatalyst loading) was used as the working electrode, a saturated calomel electrode (SCE) was used as the reference electrode, and a Pt wire was used as the counter electrode. The catalyst ink (12 μL) was loaded onto the polished GC electrode surface by dispersing 1 mg of the as-prepared catalyst in 1 mL of a 5 wt% Nafion–ethanol–water mixture. Electrochemical experiments monitoring the ORR were conducted in an O<sub>2</sub> saturated 0.1 M KOH aqueous solution at a scan rate of 10 mV s<sup>-1</sup> at room temperature. Rotating disk electrode (RDE) measurements were obtained at different speeds (from 700 to 2500 rpm). Koutecky–Levich (K–L) plots were analyzed at various electrode potentials. The slopes of the best linear fit lines were used to calculate the number of electrons transferred (n) based on the K–L equation as follows [29]:

$$\frac{1}{j} = \frac{1}{j_k} + \frac{1}{B\omega^{1/2}} \quad (1)$$

$$B = 0.2nFC(D)^{2/3}\nu^{-1/6}, \quad (2)$$

where j and j<sub>k</sub> are the measured current density and the kinetic limiting current density, respectively, B is the Levich slope, ω is the rotation speed, n is the total number of electrons transferred per O<sub>2</sub> molecule, F is the Faraday constant (F=96,485 C mol<sup>-1</sup>), C is the bulk O<sub>2</sub> concentration in the electrolyte, D is the O<sub>2</sub> diffusion coefficient in a 0.1 M KOH aqueous solution, and ν is the kinematic viscosity of the electrolyte.

### 2.4. MFC configuration and operation

The air-cathode, single-chamber MFCs were set up as previously described by Yuan et al. [30]. A carbon cloth (7.0 cm<sup>2</sup>, type A) purchased from Fuel Cell Earth LLC Inc. (USA) was used as the anode. The cathode catalytic layer was coated with either as-prepared

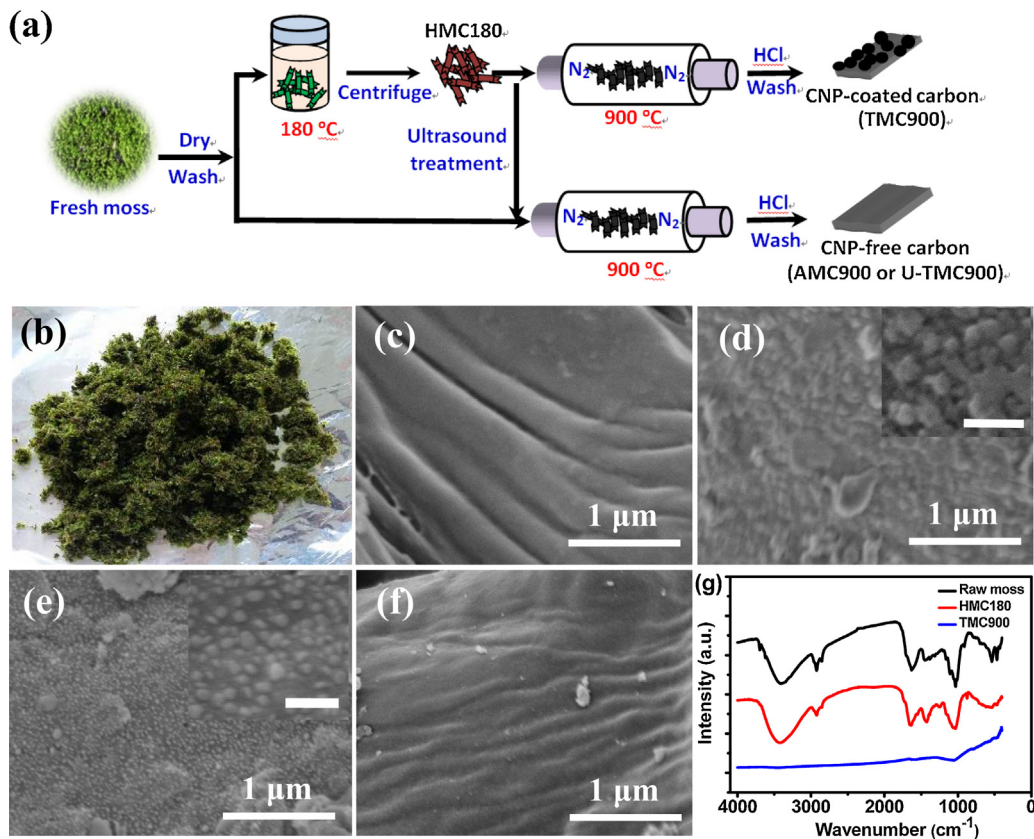


**Fig. 1.** Schematic procedure for the preparation of CNP-coated, N-doped porous carbon materials from moss (a); image of the obtained plant moss from local concrete walls (b); SEM image of the raw moss (c); SEM images of the moss-derived carbon after hydrothermal carbonization (HMC180) (d, Inset: a high resolution SEM image of HMC180, scale bar: 100 nm); SEM images of the hydrothermal carbonized moss after further annealing at 900 °C (TMC900) (e, Inset: a high resolution SEM image of TMC900, scale bar: 100 nm); SEM image of the moss-derived carbon prepared directly from annealing at 900 °C (AMC900) (f); FTIR spectra of TMC900, HMC180 and raw moss (g).

carbon materials or Pt/C. The catalyst dosage on the cathode surface was 2 mg/cm<sup>2</sup> for the carbon materials and 0.5 mg/cm<sup>2</sup> for Pt (20% Pt/C); a Nafion solution (5%, HESEN, China) was used as the binder. MFCs with a liquid volume of 28 mL were inoculated with 5.0 mL of activated anaerobic sludge (Liede Sewage Treatment Plant, Guangzhou, China) and 23 mL of 1 g/L sodium acetate solution in a 50 mM phosphate buffer (pH 7.0) containing a 12.5 mL/L mineral solution and a 5 mL/L vitamin solution. The voltages of the MFCs were recorded using a 16-channel voltage collection instrument (AD8223, Ruibohua Control Technology Co., Ltd., Beijing, China) with a 1 k $\Omega$  external resistance. The polarization curve was constructed by discharging the cell with external loads of various resistances. All of the tests were conducted in batch mode in a 30 °C incubator. The power was normalized by the projected surface area of the cathode (7.0 cm<sup>2</sup>). All of the tests were conducted in triplicate, and the mean values are presented in this study.

### 3. Results and discussion

#### 3.1. Preparation of CNP-coated, N-doped porous biocarbon materials from moss

A scheme for the preparation of the moss-derived biocarbon materials is shown in Fig. 1a. This scheme includes two heat treatment steps in the absence of chemical agents. In a typical synthesis, the moss-derived carbon materials were obtained in a yield of approximately 65% by a facile hydrothermal process at 180 °C, and the resulting brown pellets were then annealed at 900 °C in a  $N_2$  atmosphere to produce TMC900 (yield approximately 52%). After hydrothermal treatment, the supernatants were collected

and further surveyed. The final yield of the biocarbon catalyst from the moss was approximately 34%; this yield is comparative to that of biomass-derived carbon materials presented in the literature [31,32]. These biocarbon materials were produced using inexpensive and readily available plant moss, and the synthetic strategy is economical, user-friendly, and amenable to scale-up. It represents a “green” approach for producing highly efficient electrocatalysts. As controls, CNP-free biocarbons were also prepared from moss using a one-step heat treatment process at 900 °C to produce AMC900, and an ultrasound treatment was combined with a two-step heat treatment procedure to produce U-TMC900.

The photo in Fig. 1b shows the raw moss collected from a local field. Figs. 1c and S2 (Supporting information) show the surface morphology of the air-dried raw moss, which was smooth and unwrinkled. After hydrothermal treatment at 180 °C, round nanoparticles were distributed over the wrinkled surface as shown in Figs. 1d and S2. The diameter of the nanoparticles was ~20 nm as shown in the insert of Fig. 1d. After a subsequent annealing treatment at 900 °C, the nanoparticles became more visible and smaller (Fig. 1e and Fig. S2e); these particles (~10 nm in size) are seen in the insert of Fig. 1e. CNPs were not observed on the AMC900 samples (Figs. 1f and S2f), demonstrating that the CNPs were synthesized during the hydrothermal process. However, it is worth mentioning that the CNPs were dissociated from the HMC180 after the ultrasound treatment (Fig. S2g). The resultant supernatant after the ultrasound treatment showed bright blue luminescence under a UV beam of 365 nm (Inset of Fig. S2g), also confirming the presence of carbon nanodots in the aqueous solution that are dissociated from the HMC180. CNP-free TMC900 (U-TMC900) could be achieved after further annealing CNP-free HMC180 at 900 °C (Fig. S2h). The

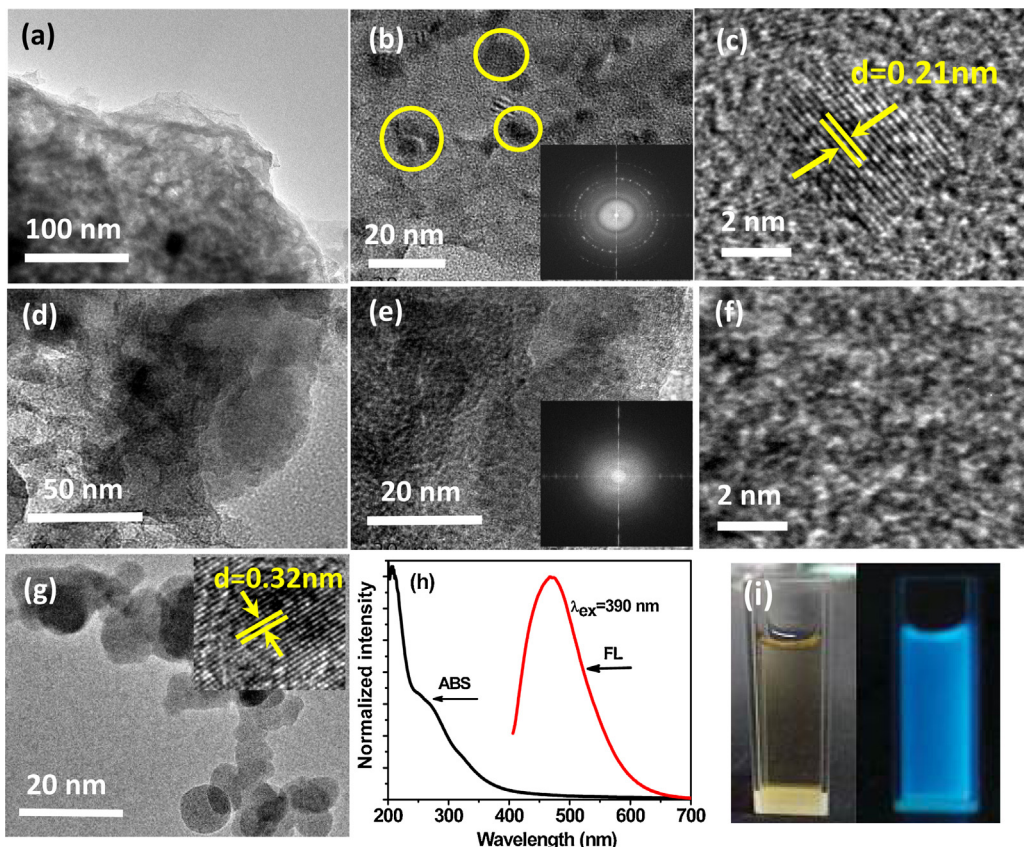


**Fig. 2.** TEM (a and b) images of TMC900 (Inset: a SEAD pattern of TMC900); HRTEM images of a single CNP on TMC900 (c); TEM (d and e) images of AMC900 (Inset: SEAD pattern of AMC900); HRTEM image of AMC900 (f); TEM image of CNPs obtained from the solution after the moss was processed by hydrothermal carbonization (g, Inset: HRTEM image of a single CNP); optical properties of the moss-derived CNPs (h); photograph of the obtained CNPs under white light (left) and UV beam of 365 nm (right) (i).

morphology of the nanoparticles was also characterized by TEM and HRTEM. The TEM images clearly show that TMC900 (Fig. 2a and b) possessed graphene-like features with a highly developed porous network and distribution of nanoparticles. Selected area electron diffraction (SAED) of the TMC900 sample in Fig. 2b shows a ring-like diffraction pattern with dispersed bright spots, which can be partially attributed to the existence of CNPs with abundant edges [33]. High-resolution TEM (HRTEM) imaging (Fig. 2c) reveals that the lattice spacing of the CNPs is 0.21 nm, which corresponds to the (100) crystal face of graphite [34]. By contrast, TEM images reveal that the surfaces of the AMC900 samples are not decorated with nanoparticles and only exhibit small porous networks (Fig. 2d and e). SAED of the AMC900 sample in Fig. 2e shows diffuse rings in the diffraction pattern, which indicates that the sample is amorphous [34]. HRTEM analysis (Fig. 2f) further confirms the distribution of porous networks and the absence of CNPs on the AMC900 sample. Numerous studies have demonstrated that CNPs, known as carbon dots, can be synthesized via hydrothermal carbonization of various biomasses (e.g., *Gastrodia elata*, orange peel, Zoysiagrass, coffee, and soybean, among others) because of their carbohydrate, protein and amino acid contents [35–39]. This method represents a green method for the production of functional CNPs. Using the same principle, carbon-enriched organic molecules were released from the moss and subsequently carbonized as carbon nanoparticles. As shown in Fig. 2g, CNPs (less than 20 nm in size) were observed in the supernatant. Note that the CNPs in the aqueous solution are the same size as those coated on the surface of HMC180, suggesting that the CNPs are generated from the moss and then self-assembled onto HMC180 during the hydrothermal treatment. The HRTEM image in Fig. 2g reveals that the lattice spacing of the CNPs is 0.32 nm, corresponding to few-layer CNPs or graphitic crystal-

lites [33]. Fig. 2h and i shows optical properties of the moss-derived CNPs. An aqueous solution of CNPs showed an obvious feature centered at approximately 266 nm in the UV/vis absorption spectrum. When excited at 390 nm, the CNPs in this aqueous solution showed a strong fluorescence emission peak centered at 469 nm (Fig. 2h), and showed bright blue luminescence under a UV beam of 365 nm (Fig. 2i). Note that the CNPs obtained from the ultrasound-treated HMC180 showed the similar optical property (Fig. S2 g), which further demonstrated that the CNPs packed on the HMC180 was likely generated from the moss during hydrothermal treatment.

### 3.2. Characterization of the as-prepared carbon materials

The conversion of raw moss into carbonaceous materials was also confirmed by XRD, FTIR and XPS measurements. Fig. 1g shows the FTIR spectra of the raw moss and carbonized materials. The raw moss possessed abundant carboxyl and hydroxyl groups, indicated by the presence of absorption bands in the region between 300 and 4000 cm<sup>-1</sup>. An absorption band related to the stretching of the N–H bonds of organic compounds is also seen in this region of the spectrum. The absorption bands at 1545 and 1650 cm<sup>-1</sup> were related to the C–O vibration of the primary amides [40]. The FTIR spectrum of HMC180 was nearly identical to that of the moss before it was treated at 180 °C, indicative of incomplete carbonization of the moss at this temperature. When the carbonaceous materials were further treated at 900 °C, bands typical of carbonized moss were observed; the carbon materials showed a broad continuum absorption with only a few peaks between 500 and 4000 cm<sup>-1</sup>, resulting from the excitation of the “free” conduction electrons [41].

XPS measurements were also conducted to elucidate the chemical structure of the as-prepared carbonaceous materials (Figs. 3a

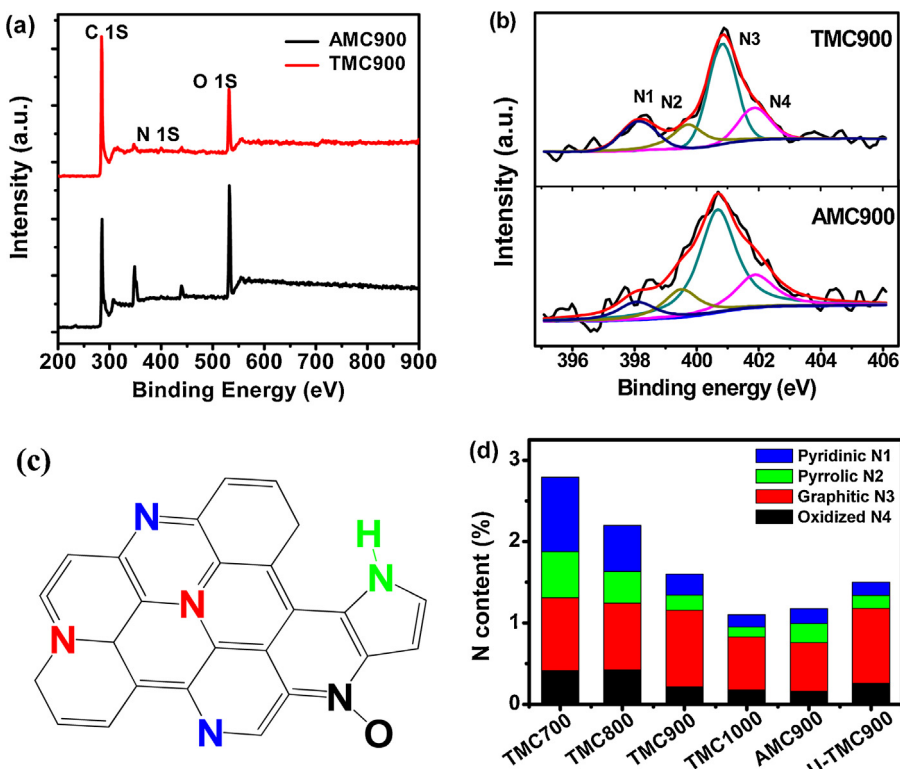


**Fig. 3.** Full-scan XPS of AMC900 and TMC900 (a); high resolution N 1s XPS scan of AMC900 and TMC900 (d); representative N doping in the as-prepared carbon materials (c); the content of the four types of nitrogen in the moss-derived carbon materials (d).

and S3). The XPS survey spectra revealed the presence of C, O, and N in the carbon samples. According to the XPS data (Table S1), the atomic percentage of C (76.5%), O (15.3%), and N (1.6%) was reached for TMC900. In the high-resolution C1s spectrum of TMC900, the dominant peak at 284.6 eV can be attributed to the C–C bond of the  $\text{sp}^2$  graphitic carbon, whereas the peak at 285.8 eV can be attributed to the C–O or C–N bonds [42]. Note that fewer peaks and higher C–C bond peak intensities were observed for TMC900 compared to HMC180. The increase in temperature from 180 to 900 °C resulted in an increase in the number of CC bonds of graphitic carbon. In the high-resolution O1s spectra of TMC900 and HMC180, two peaks were observed, which were identified as O–C bonds (532.5–532.8 eV) and O–C bonds (531.1–531.5 eV), respectively [43]. TMC900 presented mostly O–C groups, whereas HMC180 presented mostly O–C groups. By comparing the relative intensities of the two peaks, it was found that the oxygen-containing groups changed from O–C to O–C after heating to 900 °C [44]. From the high-resolution N1s spectra of the samples (Figs. 3b and S4), it is evident that pyridinic (N1, 398.1 eV), pyrrolic (N2, 399.7 eV), graphitic (N3, 400.8 eV) and oxidized (N4, 402.0 eV) nitrogen-containing groups were doped on the resulting carbon materials. The densities and distributions of the N groups on the TMC900 samples were evaluated by quantitative energy dispersive X-ray spectroscopy (EDS). As seen in Fig. S5, the element N was found to be homogeneously distributed over the surface. The bonding configurations of these four N groups are schematically shown in Fig. 3c. To investigate the transformation of the N groups during pyrolysis, the percentages of the N groups in the carbon materials prepared at different temperatures were plotted (Fig. 3d). The total N percentage decreased as the temperature increased. Higher percentages of pyridinic and pyrrolic N were achieved using relatively low temperatures, and higher percentages of graphitic N were observed using relatively high temperatures, suggesting that more pyridinic and pyrrolic N is transformed into graphitic N

as the temperature increases. Moreover, note that TMC900 has a higher total N content than AMC900 and U-TMC900, which can be attributed to the presence of the N-doped CNPs on the surface of the TMC900 (Table S1). As shown in Fig. S6, the XPS spectra of the CNPs collected from the supernatant of the hydrothermal products reveals that C, O, and N are the dominant elements, confirming the production of the N-doped CNPs. The N 1s spectrum also showed the presence of pyridinic, pyrrolic, graphitic and oxidized N groups on the CNPs (Fig. S6).

Fig. 4a and b shows the  $\text{N}_2$  adsorption–desorption isotherms and pore size distributions of the as-prepared carbon materials. Table S1 shows the BET surface areas, total pore volumes and pore sizes of the carbon materials prepared at various temperatures. Among the carbon materials, TMC1000 exhibited the highest surface area ( $420.1 \text{ m}^2 \text{ g}^{-1}$ ), the largest total pore volume ( $0.52 \text{ cm}^3 \text{ g}^{-1}$ ), and the largest pore diameter (4.5 nm). The surface area, total pore volume, and pore diameter of TMC900 was  $409.5 \text{ m}^2 \text{ g}^{-1}$ ,  $1.08 \text{ cm}^3 \text{ g}^{-1}$ , and 4.2 nm, respectively; these values are significantly higher than those of AMC900. The surface area of TMC900 was also found to be higher than that of U-TMC900 (Fig. S2i and Table S1); however, these samples have similar total pore volumes and pore diameters, suggesting that the CNPs contribute to the high surface area of TMC900. Note that the BET surface area of TMC900 was also significantly larger than that of the moss-derived carbon material ( $271.2 \text{ m}^2 \text{ g}^{-1}$ ) obtained by Ding et al., who integrated pyrolysis at 900 °C and air activation at 300 °C to convert peat moss into porous carbon nanosheets [27]. The larger BET surface area of TMC900 can be attributed to the CNP coating, while the higher pore volume and larger pore size can be attributed to the release of organic molecules from the moss during hydrothermal treatment [22]. As depicted in Fig. 4c, organic molecules, such as carbohydrates and amino acids, can be released from the moss, while the nanopores remain on the moss-derived carbon during the hydrothermal process. This phenomenon was indicated by the increased porous structure of the

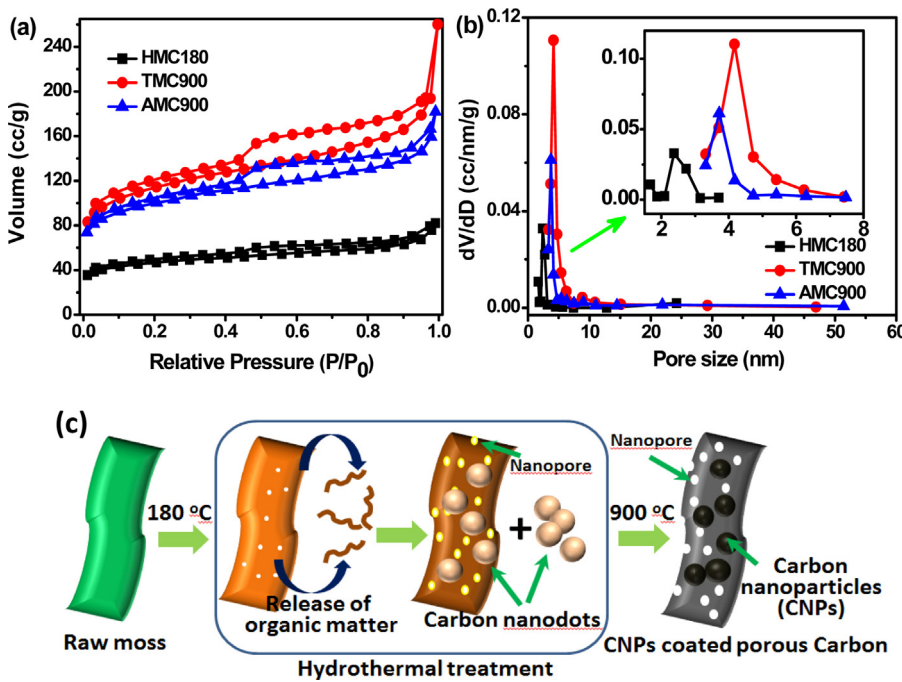


**Fig. 4.** (a) Nitrogen adsorption–desorption isotherms for HMC180, TMC900 and AMC900; (b) pore size distributions for HMC180, TMC900 and AMC900; (c) proposed mechanism for the formation of CNPs and nanopores on the as-prepared carbon materials.

U-TMC900 sample compared to that of the AMC900 sample (Table S1). Chemical measurements revealed that hydroxyl and carbonyl functional groups were prevalent on the CNP and the moss-derived carbon matrices. The strong interactions between the hydroxyl and carbonyl functional groups of the CNPs and the moss-derived carbon materials ensured that their packing was compact [45].

### 3.3. Electrocatalytic activities of TMC900 in the oxygen reduction reaction

The as-prepared CNP-coated, N-doped porous carbon materials were evaluated for electrocatalytic activity in the ORR. The cyclic voltammogram (CV) of the TMC900 electrode showed the typical pseudo-capacitive behavior of heteroatom-doped graphitic carbon when the electrolyte was saturated with  $N_2$  (Fig. 5a). By contrast, a well-defined cathodic current peak at 0.76 V vs. RHE resulting from  $O_2$  reduction was observed from the  $O_2$  saturated KOH solution; this value was only slightly more negative than that resulting from the use of the Pt/C catalyst. To further understand the kinetics of the ORR on the TMC900 in terms of onset and half-wave potentials (Fig. S7), rotating disk electrode (RDE) voltammograms were obtained by scanning the potential from 1.22 to 0.22 V vs. RHE at a scan rate of 10 mV/s in an  $O_2$ -saturated 0.1 M KOH solution. The CNP-free AMC900 sample and U-TMC900 sample were found to have onset potentials of 0.871 and 0.912 V (vs. RHE), respectively, and half-wave potentials of 0.762 V and 0.791 V (vs. RHE), respectively (Fig. 5b). Interestingly, TMC900 showed substantially higher activity in the ORR, with an onset potential of 0.935 V (vs. RHE) and a half-wave potential of 0.832 V (vs. RHE), suggesting that CNP doping plays an important role in catalytic activity. The half-wave potential of TMC900 was only 20 mV less than that of Pt/C, and its limited diffusion current was higher than that of Pt/C, demonstrating that TMC900 could be a promising catalyst in the ORR. The limited current density of TMC900 increased with increasing rotation speed (Fig. 5c), suggesting that the diffusion distance was shorter at higher speeds. This finding is consistent with those of other studies [46,47]. Fig. 5d profiles the corresponding K-L plots

that demonstrate the inverse current density ( $j^{-1}$ ) as a function of the inverse of the square root of the rotation speed ( $\omega^{-1/2}$ ) at different potential values. In the K-L plots of the TMC900 electrode, the relationship between  $1/j$  and  $\omega^{-1/2}$  was linear between 0.71 V and 0.51 V vs. RHE. According to the K-L equations, the number of electrons transferred during the ORR process for TMC900 was close to four, indicating that the ORR process occurred via a four-electron transfer pathway. However, the calculated number of electrons transferred by AMC and U-TMC900 was close to 3.0 ~ 3.5, indicating that the ORR process occurred via a combined two- and four-electron transfer pathway (Fig. S8). By comparing the ORR performance of the CNP-free biocarbons (AMC900 and U-TMC900) and TMC900, the benefit of the CNP coating on TMC900 was revealed.

The annealing temperature had a profound effect on the catalytic activities of the biomass-derived carbon materials in the ORR. As shown in Fig. S9, the moss-derived carbon prepared at 900 °C clearly outperformed the carbon materials derived at other temperatures. According to previous studies, nitrogen functional groups (i.e., pyridinic N, pyrrolic N and graphitic N) introduced into the carbon lattice can change not only the carbon surface chemistry but also its electronic structure. The doped N with a lone electron pair can create positive charge density on the adjacent C atoms, resulting in highly favorable  $O_2$  adsorption and subsequently high ORR activity [48]. The catalytic activity of the resulting carbon materials increased with increasing pyrolysis temperature between 700 and 900 °C, indicated by the positively shifted onset potential (Fig. S9). This increase in catalytic activity with pyrolysis temperature is in accordance with the increase in graphitic N content. This result provides additional evidence that graphitic N is the N functionality that may be responsible for the ORR catalytic activity. However, pyrolysis at temperatures higher than 900 °C causes the decomposition of certain N functionalities and results in a decrease in catalytic activity. Therefore, the highest catalytic activity is obtained at an intermediate temperature of 900 °C; this result has also been seen in other studies [19,49]. The active sites for the ORR on the TMC900 were further determined by examining the nitrogen functionalities before and after the ORR. As shown in Fig. S10, the XPS analy-

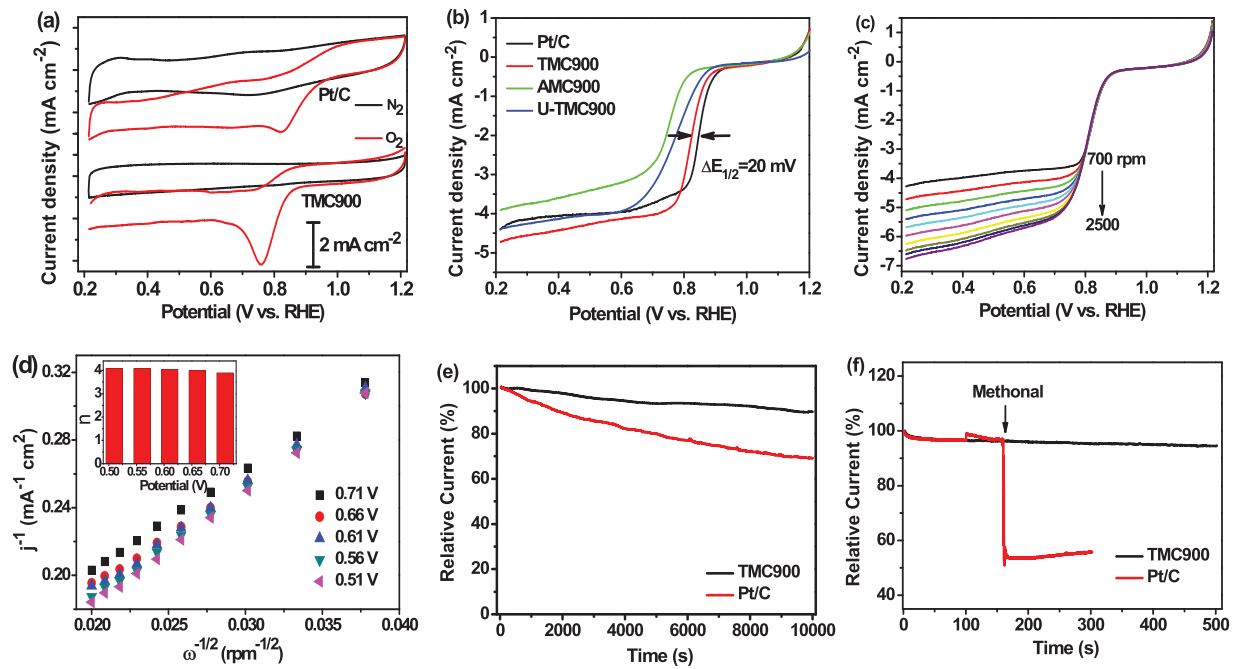


**Fig. 5.** (a) CV curves for TMC900 in  $N_2$ -saturated and  $O_2$ -saturated 0.1 M KOH solutions at a scan rate of  $10 \text{ mV s}^{-1}$ ; (b) RDE curves for TMC900, AMC900, U-TMC900 and Pt/C in  $O_2$ -saturated 0.1 M KOH solutions at a scan rate of  $10 \text{ mV s}^{-1}$  and a rotation speed of 1100 rpm; (c) RDE curves of TMC900 at different rotation rates, (d) K-L plots at different potentials for TMC900 (Inset: the calculated number of electrons transferred ( $n$ )); (e) chronoamperometric responses of the TMC900 and Pt/C electrodes at  $-0.35 \text{ V}$  (vs. SCE) in  $O_2$ -saturated 0.1 M KOH solutions at a rotation rate of 1100 rpm, normalized to the initial current responses; (f) chronoamperometric responses to the injection of 1 M methanol into an  $O_2$ -saturated 0.1 M KOH solution at the TMC900 and Pt/C electrodes.

sis shows that the pyridinic and pyrrolic nitrogen peaks decrease, while the graphitic nitrogen content holds steady. The oxidized nitrogen peak increases after the ORR. In general, pyrrolic nitrogen is prone to oxidation during the ORR process, which will cause the loss of pyrrolic nitrogen [50]. The observed decrease in pyridinic nitrogen may be due to the  $-\text{OH}$ -attached pyridinic nitrogen after the electrochemical reaction, which demonstrates that pyridinic N may play an important role in the ORR process [51]. Together with the above-mentioned conclusion, both graphitic and pyridinic nitrogen probably contribute to the catalytic properties of the TMC900 samples. As previously reported, graphitic N can greatly increase the limiting current density, whereas pyridinic N might change the ORR reaction mechanism from a  $2\text{e}^-$ -dominated process to a  $4\text{e}^-$ -dominated process [52]. The catalytic activities of the TMC900 samples in the ORR (specifically, their onset potentials and electron transfer numbers ( $n$ )) are higher than those of the CNP-free AMC900 and U-TMC900 samples; whereas this sample outperformed those biomass-derived carbon catalysts that have not been subjected to activation and their performance was comparative to those biomass-derived carbon catalysts that did undergo chemical activation treatments (Table S2). These results demonstrate that our approach is capable of producing high-performance carbon catalysts for use in the ORR without the involvement of any chemical activation processes. The observed increase in catalytic activity with increasing pyrolysis temperature between 700 and  $900^\circ\text{C}$  is in agreement with the increases in the BET surface area and porous diameter (Table S1), demonstrating that the active site density is largely dependent on high surface area and porous nature. Therefore, the construction of a porous carbon material with a large exposed surface and a high content of N functionalities can provide an opportunity to achieve high-performance catalytic activity in the ORR. The CNP coating increased the surface area of TMC900 and its N content and porosity, which offered an increased number of active sites for oxygen adsorption and reduction.

Metal-free, heteroatom-doped carbon materials show superior stability and tolerance to the crossover effect compared with Pt/C catalysts; this behavior was also observed for TMC900. For example, the ORR current density produced by TMC900 decreased by only 8% as examined by chronoamperometric measurements over 10,000 s of continuous operation at a constant voltage of  $-0.35 \text{ V}$  vs. SCE, while the Pt/C catalyst exhibited a 30% decrease in current density under similar testing conditions (Fig. 5e). The durability of TMC900 is comparable to other metal-free carbon catalysts derived from various biomasses (Table S2). Moreover, the presence of 3 M methanol did not affect the catalytic ORR of TMC900 (Fig. 5f), whereas a strong amperometric response of Pt/C was observed as a result of methanol oxidation. This result suggests that TMC900 exhibit a high selectivity towards the ORR with a remarkable tolerance for crossover effects.

#### 3.4. Application of TMC900 as the cathode catalyst in a microbial fuel cell

Microbial fuel cells (MFCs) have been intensively researched in recent years as an emerging renewable energy technology due to their wide range of applications. They can be used in applications involving wastewater treatment, electricity generation, biohydrogen production, pollutant removal and biosensing [53,54]. However, the commercial applications of these devices have been hindered by high electrode costs and the low performance of the Pt cathode [55]. Various non-noble metal catalysts have been developed to replace the Pt component, such as transition metal macrocycles, metal oxides, and carbon materials [56–61]. Despite tremendous progress in the development of non-noble metal catalysts, the activity, stability and cost of these materials in the ORR remain substantially different than what would be desired for their use in practical applications. To evaluate the suitability of TMC900 as a replacement for the Pt component of MFC cathode catalysts, single-chamber MFCs equipped with the as-prepared

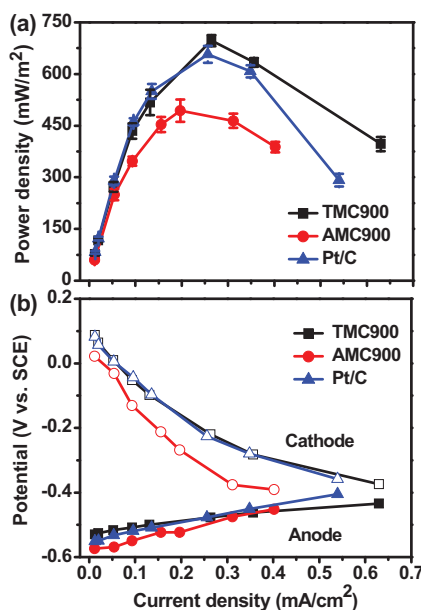


**Fig. 6.** (a) Polarization curves of MFCs with different cathodes; (b) Individual potential (vs. SCE) vs. current density curves.

catalysts were constructed. After the cell voltages were stabilized, the MFCs were subjected to polarization analyses. As shown in Fig. 6A, the MFC with the TMC900 cathode had a power density of  $703 \pm 16 \text{ mW/m}^2$ , which was slightly higher than that of the MFC with the Pt/C cathode catalyst ( $656 \pm 24 \text{ mW/m}^2$ ) and substantially higher than that of the MFC with the AMC900 cathode ( $494 \pm 32 \text{ mW/m}^2$ ). Fig. 6B shows the potential vs. current density curves for the individual cathodes and anodes. For these MFCs, the cathode potentials differed, while the anode potentials were similar, indicating that the differences in the MFCs' performance resulted primarily from variations in the catalytic activities of the cathode catalysts. It is thought that the as-prepared TMC900 has many advantages when used as the electrocatalyst in the ORR. First, the cost of TMC900 is extremely low due to its sustainable nature; the moss can be directly converted into the efficient catalyst. Second, the strategy could be easily scaled-up for catalyst production because the entire process is facile.

#### 4. Conclusion

In summary, we demonstrate a facile and effective method to produce CNP-coated, N-doped porous biocarbon materials from readily available natural moss using a combination of hydrothermal treatment and pyrolysis carbonization. The unique features of the TMC900 samples fabricated using this facile procedure include a CNP coating, inherent mesoporosity, and the presence of enriched, active N species in the carbon matrix, and these parameters result in high ORR activity and stability in alkaline media. Further, the fuel crossover effect does not come into play. The CNPs formed during the hydrothermal process as a result of the release of small organic molecules from the moss and also led to the formation of nanopores on the biocarbon. The as-prepared, CNP-coated biocarbon materials display activities in the ORR that are comparable to those of commercial Pt/C catalysts in 0.1 M KOH, and they outperform Pt/C in terms of stability and tolerance to methanol. Specifically, TMC900 exhibited good performance in MFCs with a maximum power density comparable to that of Pt/C. The present study provides a new route for the direct synthesis of a metal-free electrocatalyst with high activity and low cost from a type of biomass.

#### Acknowledgements

Financial support was provided by Guangdong Natural Science Funds for Distinguished Young Scholar(2014A030306033), and the National Natural Science Foundation of China (Grant No. 41301264 and 21277035).

#### Appendix A. Supplementary data

Supplementary data associated with this article can be found, in the online version, at <http://dx.doi.org/10.1016/j.apcatb.2015.08.035>.

#### References

- [1] B.C.H. Steele, A. Heinzel, *Nature* 414 (2001) 345–352.
- [2] K. Gong, F. Du, Z. Xia, M. Dustock, L. Dai, *Science* 323 (2009) 760–764.
- [3] Y.G. Li, M. Gong, Y.Y. Liang, J. Feng, J.E. Kim, H.L. Wang, G.S. Hong, B. Zhang, H.J. Dai, *Nat. Commun.* 4 (2013) 1805.
- [4] A. Rinaldi, B. Mecheri, V. Garavaglia, S. Licoccia, P.D. Nardo, E. Traversa, *Energy Environ. Sci.* 1 (2008) 417–429.
- [5] X. Liu, W. Li, H.Q. Yu, *Chem. Soc. Rev.* 43 (2014) 7718–7745.
- [6] H.A. Gasteiger, N.M. Markovic, *Science* 324 (2009) 48–49.
- [7] A. Gasteiger, S.S. Kocha, B. Sompalli, F.T. Wagner, *Appl. Catal. B: Environ.* 56 (2005) 9–35.
- [8] L. Dai, Y. Xue, L. Qu, H.J. Choi, J.B. Baek, *Chem. Rev.* (2015), <http://dx.doi.org/10.1021/cr50035630>.
- [9] N. Daems, X. Sheng, I.F.J. Vankelecom, P.P. Pescarmona, *J. Mater. Chem. A* 2 (2014) 4085–4110.
- [10] L. Qu, Y. Liu, J.B. Baek, L. Dai, *ACS Nano* 4 (2010) 1321–1326.
- [11] L. Feng, Y. Chen, L. Chen, *ACS Nano* 5 (2011) 9611–9618.
- [12] T. Sharifi, G. Hu, X. Jia, T. Wägberg, *ACS Nano* 6 (2012) 8904–8912.
- [13] C. Guo, C. Chen, Z. Luo, *J. Power Sources* 45 (2014) 841–845.
- [14] Z. Xiang, D. Cao, L. Huang, J. Shui, M. Wang, L. Dai, *Adv. Mater.* 26 (2014) 3315–3320.
- [15] Y. Zhang, J. Ge, L. Wang, D. Wang, F. Ding, X. Tao, W. Chen, *Sci. Rep.* 3 (2013) 2771.
- [16] H.J. Choi, S.M. Jung, J.M. Seo, D.W. Chang, L. Dai, J.B. Baek, *Nano Energy* 1 (2012) 534–551.
- [17] T. Yang, J. Liu, R. Zhou, Z. Chen, H. Xu, S. Qiao, M.J. Monteiro, *J. Mater. Chem. A* 2 (2014) 18139–18146.
- [18] Y. Wang, T.P. Fellinger, M. Antonietti, *J. Am. Chem. Soc.* 133 (2011) 206–209.
- [19] M. Song, H.Y. Park, D.S. Yang, D. Bhattacharjya, J. Yu, *ChemSusChem* 7 (2014) 1755–1763.
- [20] S. Gao, K. Geng, H. Liu, X. Wei, M. Zhang, P. Wang, J. Wang, *Energy Environ. Sci.* 8 (2015) 221–229.
- [21] H. Zhu, J. Yin, X. Wang, H. Wang, X. Yang, *Adv. Funct. Mater.* 23 (2013) 1305–1312.
- [22] P. Chen, L. Wang, G. Wang, M. Gao, J. Ge, W. Yuan, Y. Shen, A. Xie, S. Yu, *Energy Environ. Sci.* 7 (2014) 4095–4103.
- [23] S. Gao, H. Fan, S. Zhang, *J. Mater. Chem. A* 2 (2014) 18263–18270.
- [24] H. Liang, Z. Wu, L. Chen, C. Li, S. Yu, *Nano Energy* 11 (2015) 366–376.
- [25] R. Wang, H. Wang, T. Zhou, J. Key, Y. Ma, Z. Zhang, Q. Wang, S. Ji, *J. Power Sources* 274 (2015) 741–747.
- [26] K. Yoshikawa, P.P. Overduin, J.W. Harden, *Permafrost Periglac. Process.* 15 (2004) 309–318.
- [27] J. Ding, H. Wang, Z. Li, A. Kohandehghan, K. Cui, Z. Xu, B. Zahiri, X. Tan, E.M. Lotfabad, B.C. Olsen, D. Mitlin, *ACS Nano* 7 (2013) 11004–11015.
- [28] W.A.P. Black, W.J. Cornhill, F.N. Woodward, *J. Appl. Chem.* 5 (1955) 484–492.
- [29] S. Yang, L. Zhi, K. Tang, X. Feng, J. Maier, K. Müllen, *Adv. Funct. Mater.* 22 (2012) 3634–3640.
- [30] Y. Yuan, S.G. Zhou, Y. Liu, J.H. Tang, *Environ. Sci. Technol.* 47 (2013) 14525–14532.
- [31] D.J. Suh, J.H. Choi, H.C. Woo, *Chem. Eng. Trans.* 37 (2014) 121–126.
- [32] L. Zhao, X. Cao, W. Zheng, Y. Kan, *PLoS One* 9 (2014) e115373.
- [33] C. Hu, C. Yu, M. Li, X. Wang, Q. Dong, G. Wang, J. Qiu, *Chem. Commun.* 51 (2015) 3419–3422.
- [34] J. Wang, C. Wang, S. Chen, *Angew. Chem. Int. Ed.* 51 (2012) 9297–9301.
- [35] S. Gao, H. Fan, Y. Chen, L. Li, Y. Bando, D. Golberg, *Nano Energy* 2 (2013) 1261–1270.
- [36] A. Prasannan, T. Imae, *Ind. Eng. Chem. Res.* 52 (2013) 15673–15678.
- [37] D. Jiang, Y. Zhang, M. Huang, J. Liu, J. Wan, H. Chu, M. Chen, *J. Electroanal. Chem.* 728 (2014) 26–33.
- [38] P.C. Hsu, Z.Y. Shih, C.H. Lee, H.T. Chang, *Green Chem.* 14 (2012) 917–920.
- [39] C.Z. Zhu, J.F. Zhai, S.J. Dong, *Chem. Commun.* 48 (2012) 9367–9369.
- [40] J.O. Silva, G.R. Filho, C.S. Meireles, S.D. Ribeiro, J.G. Vieira, C.V. Silva, D.A. Cerqueira, *Thermochim. Acta* 528 (2012) 72–75.
- [41] J.J. Langer, S. Golczak, P.D. Stab, *Polym. Degrad. Stab.* 92 (2007) 330–334.
- [42] T.I.T. Okpalugo, P. Papakonstantinou, H. Murphy, J. McLaughlin, N.M.D. Brown, *Carbon* 43 (2005) 153–161.

- [43] V. Datsyuk, M. Kalyva, K. Papagelis, J. Parthenios, D. Tasis, A. Siokou, I. Kallitsis, C. Gallois, Carbon 46 (2008) 833–840.
- [44] A. Bagri, C. Mattevi, M. Acik, Y.J. Chabal, M. Chhowalla, V.B. Shenoy, Nat. Chem. 2 (2010) 581–587.
- [45] H. Fei, R. Ye, G. Ye, Y. Gong, Z. Peng, X. Fan, E.L.G. Samuel, P.M. Ajayan, J.M. Tour, ACS Nano 8 (2014) 10837–10843.
- [46] J. Chen, X. Wang, X. Cui, G. Yang, W. Zheng, Chem. Commun. 50 (2014) 557–559.
- [47] P. Zhang, F. Sun, Z. Xiang, Z. Shen, J. Yun, D. Cao, Energy Environ. Sci. 7 (2014) 442–450.
- [48] H. Zhang, Y. Wang, D. Wang, Y. Li, X. Liu, P. Liu, H. Yang, T. An, Z. Tang, H. Zhao, Small 10 (2014) 3371–3378.
- [49] Y. Li, H. Zhang, Y. Wang, P. Liu, H. Yang, X. Yao, D. Wang, Z. Tang, H. Zhao, Energy Environ. Sci. 7 (2014) 3720–3726.
- [50] B. Xiao, J.P. Boudou, K. Thomas, Langmuir 21 (2005) 3400–3409.
- [51] T. Xing, Y. Zheng, L.H. Li, B.C.C. Cowie, D. Gunzelmann, S.Z. Qiao, S.M. Huang, Y. Chen, ACS Nano 8 (2014) 6856–6862.
- [52] L. Lai, J.R. Potts, D. Zhan, L. Wang, C.K. Poh, C. Tang, H. Gong, Z. Shen, J. Lin, R.S. Ruoff, Energy Environ. Sci. 5 (2012) 7936–7942.
- [53] B.E. Logan, J.M. Regan, Environ. Sci. Technol. 40 (2006) 5172–5180.
- [54] W. Li, H. Yu, Z. He, Energy Environ. Sci. 7 (2014) 911–924.
- [55] B.E. Logan, Appl. Microbiol. Biotechnol. 85 (2010) 1665–1671.
- [56] X.W. Liu, W.W. Li, H.Q. Yu, Chem. Soc. Rev. 43 (2014) 7718–7745.
- [57] Y. Yuan, B. Zhao, Y.W. Jeon, S.G. Zhong, S. Kim, Bioresour. Technol. 102 (2011) 5849–5854.
- [58] Y. Zhao, K. Watanabe, K. Hashimoto, J. Am. Chem. Soc. 134 (2012) 19528–19531.
- [59] L. Zhang, C. Liu, L. Zhuang, W. Li, S. Zhou, J. Zhang, Biosens. Bioelectron. 24 (2009) 2825–2829.
- [60] L. Feng, Y. Yan, Y. Chen, L. Wang, Energy Environ. Sci. 4 (2011) 1892–1899.
- [61] X. Zhang, X. Xia, I. Ivanov, X. Huang, B.E. Logan, Environ. Sci. Technol. 48 (2014) 2075–2081.